Ergodicity in wave-wave diffraction

1999 J. Phys. A: Math. Gen. 32 3571

(http://iopscience.iop.org/0305-4470/32/19/308)

J. Phys. A: Math. Gen. **32** (1999) 3571–3582. Printed in the UK PII: S0305-4470(99)00757-X

Ergodicity in wave–wave diffraction

M V Berry† and D H J O'Dell‡

† H H Wills Physics Laboratory, Tyndall Avenue, Bristol BS8 1TL, UK
‡ Department of Chemical Physics, Weizmann Institute, Rehovot 76100, Israel

Received 11 January 1999

Abstract. Ray propagation over long distances through a sinusoidal volume grating, where the refractive index varies perpendicular to the direction of incidence, is characterized by a proliferation of caustics. These dominate the distribution of directions (momentum density) of emerging rays. For this integrable system with one-dimensional transverse motion, the ergodic average of the momentum density is calculated exactly. For the corresponding waves, the intensities of the diffracted beams are calculated from the Raman–Nath equation. In the limit when a semiclassical parameter is small, the long-distance average agrees very well with the ergodic ray momentum density. Semiclassical scalings of the fluctuations of beam intensities about the ergodic average are predicted for the caustic curves and their cusp points.

1. Introduction

We will consider waves with vacuum wavenumber k, travelling in the ξ direction, incident normally on a medium that varies periodically and weakly in the η direction; thus the refractive index of this 'volume grating' is

$$n(\eta) = n_0 + n_1 \cos q\eta \qquad (n_1 \ll n_0). \tag{1}$$

This is an old problem. Originally it described the diffraction of light by ultrasound (see Berry (1966) for a review to 1966); now it has re-emerged in the diffraction of beams of atoms by beams of light (Adams *et al* 1994), with $n(\eta) = \sqrt{(1 - V(\eta)/E)}$, where E is the energy of the atoms and $V(\eta)$ the potential energy of their interaction with the light. The waves leaving the medium after travelling a distance ξ will consist of many Bragg-diffracted beams, travelling in directions making angles $\sin^{-1}(mq/k)$ to the ξ axis (m integer); we wish to calculate their intensities $I_m(\xi)$.

Here our emphasis will be on the limit of large ξ and short wavelength, where familiar approximations—perturbation, semiclassical, finitely-many beams—break down. The difficulty arises because of the proliferation of caustics with increasing ξ. Our main point will be that although the $I_m(\xi)$ fluctuate strongly with ξ their average over short ranges of ξ can be calculated accurately by ergodic averaging over the 'whorls' generated by the family of rays, as envisaged by Berry and Balazs (1979). A related application of ergodicity justifies commonly-used approximations in the theory of particle channelling (Ellison and Guinn 1976, Adams *et al* 1994).

0305-4470/99/193571+12$19.50

2. Rays, whorls and caustics

The simplest way to calculate the rays, regarded as curves $\eta(\xi)$, is from Snell's law: if $\mathrm{d}\eta(\xi)/\mathrm{d}\xi \equiv \tan\alpha(\xi)$, then

$$n(\eta)\cos\alpha(\xi) = \text{constant} = n(\eta_0)\cos\alpha(0) \tag{2}$$

where η_0 labels the rays in the family by the height at which they enter the medium. Incorporating the initial condition $(\mathrm{d}\eta(\xi)/\mathrm{d}\xi)(\xi = 0) = 0$ (normal incidence) enables (2) to be written

$$\left(\frac{\mathrm{d}\eta}{\mathrm{d}\xi}\right)^2 = \left(\frac{n(\eta)}{n(\eta_0)}\right)^2 - 1 \approx 4\frac{n_1}{n_0}\left(\sin^2\left(\frac{1}{2}q\eta_0\right) - \sin^2\left(\frac{1}{2}q\eta\right)\right). \tag{3}$$

This enables ξ to be evaluated as an elliptic integral, whose inversion give the rays $\eta(\xi)$ as elliptic functions. Natural dimensionless variables are

$$y \equiv \frac{1}{2}q\eta \qquad x \equiv q\sqrt{\frac{n_1}{n_0}}\xi \tag{4}$$

with ranges $(0 \leqslant x < \infty, -\pi/2 \leqslant y \leqslant \pi/2)$. The rays are

$$y(x;\, y_0) = \sin^{-1}[\sin y_0\, \mathrm{sn}(x + K(\sin^2 y_0)|\sin^2 y_0)] \tag{5}$$

where the complete elliptic integral $K(m)$ and the elliptic function $\mathrm{sn}(u|m)$ are defined in Abramowitz and Stegun (1972).

As in many paraxial situations, it is helpful to think of x as a time variable, and regard the rays (5) as generated by a Hamiltonian for the one-dimensional transverse motion. The choice

$$H(y,\, p) = \tfrac{1}{2}(p^2 + \sin^2 y) \tag{6}$$

gives the rays (5) and the conjugate 'momentum', giving the direction of the rays at x,

$$p(x;\, y_0) = \frac{\mathrm{d}y(x;\, y_0)}{\mathrm{d}x} = \sin y_0\, \mathrm{cn}(x + K(\sin^2 y_0)|\sin^2 y_0) \tag{7}$$

with range $(-1 \leqslant p \leqslant 1)$. Obviously the motion is integrable, with trajectories given explicitly by (5) and (7).

Figure 1 shows the evolution of the family of rays in y and p. The y picture was first calculated by Lucas and Biquard (1932), and both were studied in detail by Nomoto (1951a). Caustics dominate, reflecting the fact that each point (x, y), and each point (x, p), can be reached by more than one ray. The caustics are pairs of smooth curves connected by cusps. These are the focal points of the small-y (harmonic-oscillator) limit of (6); the y cusps are at $x = (n + \frac{1}{2})\pi$, and the p cusps at $x = n\pi$.

The multivaluedness can be easily comprehended by phase-space pictures for different values of x (figure 2), each showing the rays in the family as a curve. For $x = 0$, the curve is a straight line along the y axis, with points labelled by y_0. Each point evolves by moving round a closed contour (energy level) of the Hamiltonian (6), but the different y_0 rotate at different speeds. Thus the initial curve coils into a whorl, winding more tightly with increasing x. We call the whorl at x the x whorl; it is represented by a phase-space density d, whose equation is

$$d(y,\, p;\, x) = \frac{1}{\pi}\int_{-\pi/2}^{\pi/2} \mathrm{d}y_0\, \delta(y - y(x;\, y_0))\delta(p - p(x;\, y_0)). \tag{8}$$

For each x, the momenta of the different rays reaching each point y are given by the intersections of the vertical line y with the x whorl, and the y caustics are the tangencies, where $\partial y/\partial y_0 = 0$. Similarly, the positions of the different rays reaching each point p are

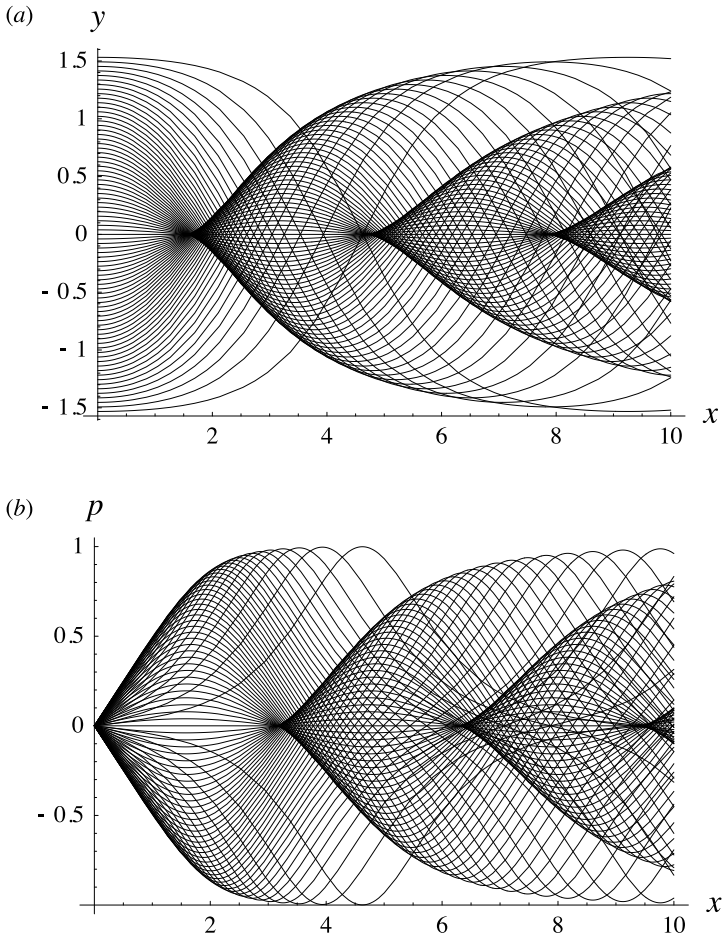

Figure 1. Rays in configuration (*a*) and momentum (*b*) space, generated from equations (5) and (7) for a range of initial heights y_0.

given by the intersections of the horizontal line p with the x whorl, and the p caustics are the tangencies, where $\partial p/\partial y_0 = 0$. Evidently caustics proliferate as x increases.

The momentum density of the ray family at x, or, equivalently, the classical far-field differential scattering cross section from a unit cell of the refractive-index profile, normalized to unity, is

$$\begin{aligned} I(p;x) &= \int_{-\pi/2}^{\pi/2} \mathrm{d}y\, d(y,p;x) \\ &= \frac{1}{\pi}\int_{-\pi/2}^{\pi/2} \mathrm{d}y_0\, \delta(p - p(x;y_0)) \\ &= \frac{1}{\pi}\sum_i \left|\frac{\partial p(x;y_0)}{\partial y_0}\right|^{-1}_{y_0=y_{0i}(p;x)} \end{aligned} \tag{9}$$

where $y_{0i}(p;x)$ are the initial heights of the rays (labelled by i) reaching p at x. Figure 3 shows momentum densities for several x. The caustic singularities, where $\partial p/\partial y_0 = 0$, are obvious,

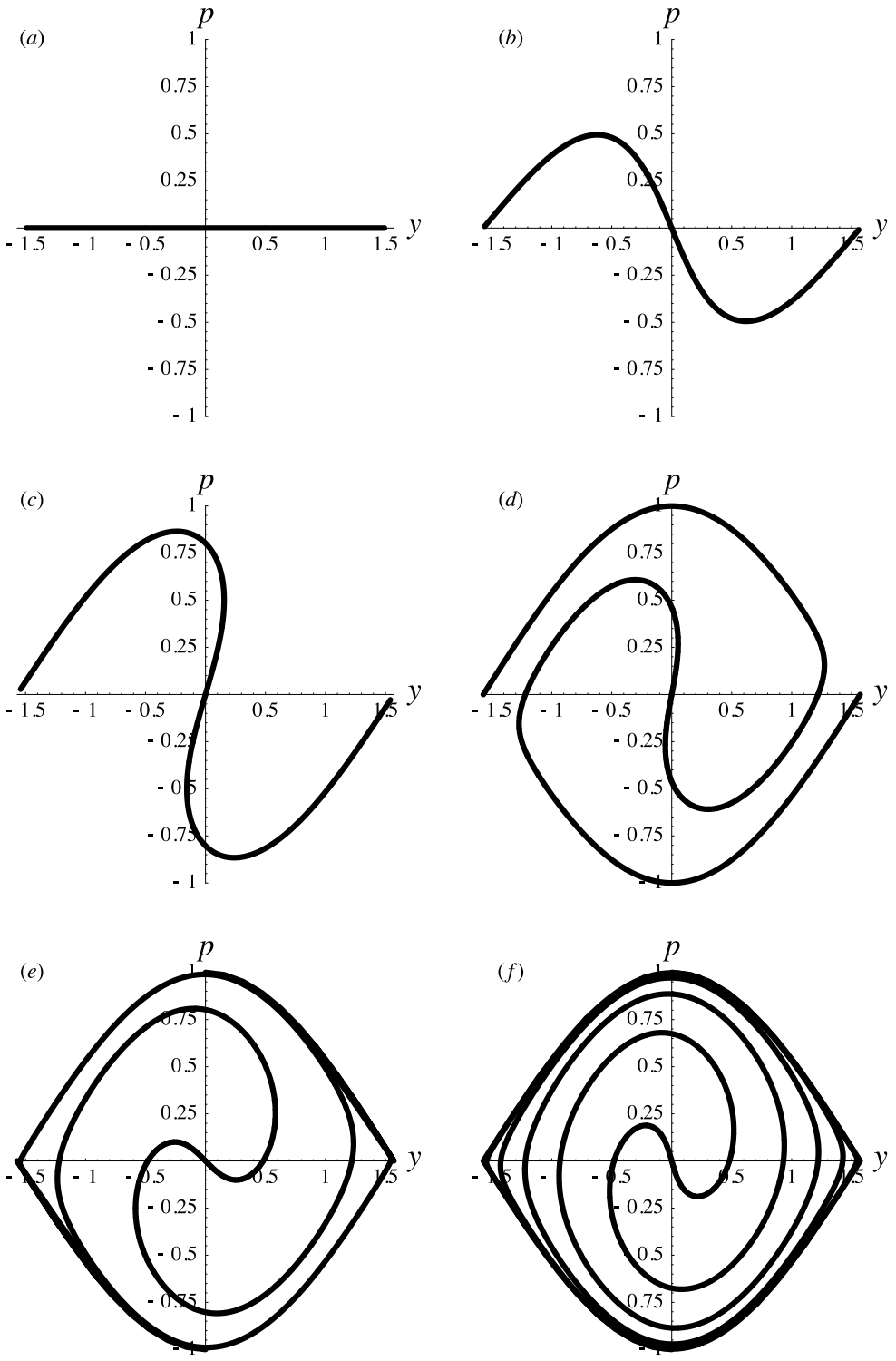

Figure 2. Whorls in phase space generated parametrically from (5) and (7) with $(-\pi/2 \leqslant y_0 \leqslant \pi/2)$, for (*a*) $x = 0$; (*b*) $x = 1$; (*c*) $x = 2$; (*d*) $x = 5$; (*e*) $x = 10$; (*f*) $x = 20$.

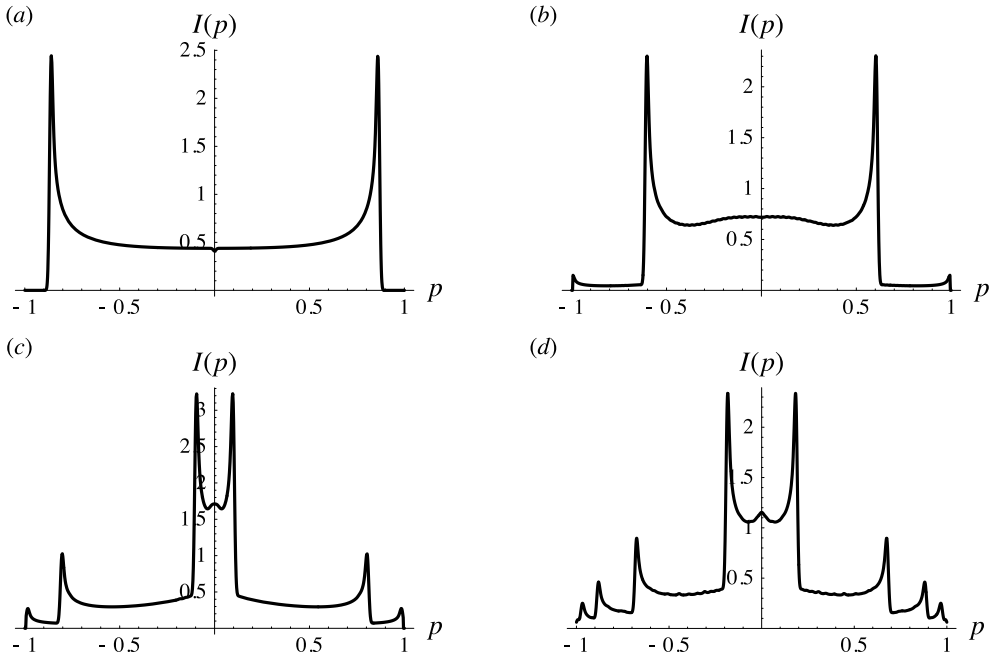

Figure 3. Momentum densities for (*a*) $x = 2$; (*b*) $x = 5$; (*c*) $x = 10$; (*d*) $x = 20$, calculated numerically from (7) and the second equation in (9) by replacing the δ function by a narrow Gaussian.

as is their proliferation with x: the number of caustics across the density at x is $2\,\mathrm{Int}(x/\pi)$. The position density, that is the ray intensity as a function of y, shows similar features.

3. Ergodicity

For very large x, the caustics can be regarded as dense, and we can study the coarse-grained momentum density, in which the singularities are smoothed away by averaging. To calculate this, we employ a three-stage process.

First, the point in each whorl associated with the ray labelled y_0 is replaced by a normalized density on the energy contour that it explores ergodically with x, that is, by the microcanonical density (normalized to unity)

$$d_{\mathrm{m}}(y,\,p;\,y_0) = \frac{\delta(H(y,\,p) - H(y_0,\,0))}{\iint \mathrm{d}y\,\mathrm{d}p\,\delta(H(y,\,p) - H(y_0,\,0))} = \frac{1}{2K(\sin^2 y_0)}\delta(p^2 + \sin^2 y - \sin^2 y_0). \tag{10}$$

Second, d_{m} is averaged over y_0, to obtain the phase-space density $W(y,\,p)$ of the smoothed x whorls for large x, normalized to unity:

$$W(y,\,p) = \frac{1}{\pi}\int_{-\pi/2}^{\pi/2} \mathrm{d}y_0\, d_{\mathrm{m}}(y,\,p;\,y_0) = \left[2\pi K(\sin^2 y + p^2)\sqrt{(\sin^2 y + p^2)(\cos^2 y - p^2)}\right]^{-1}\Theta(\cos y - |p|) \tag{11}$$

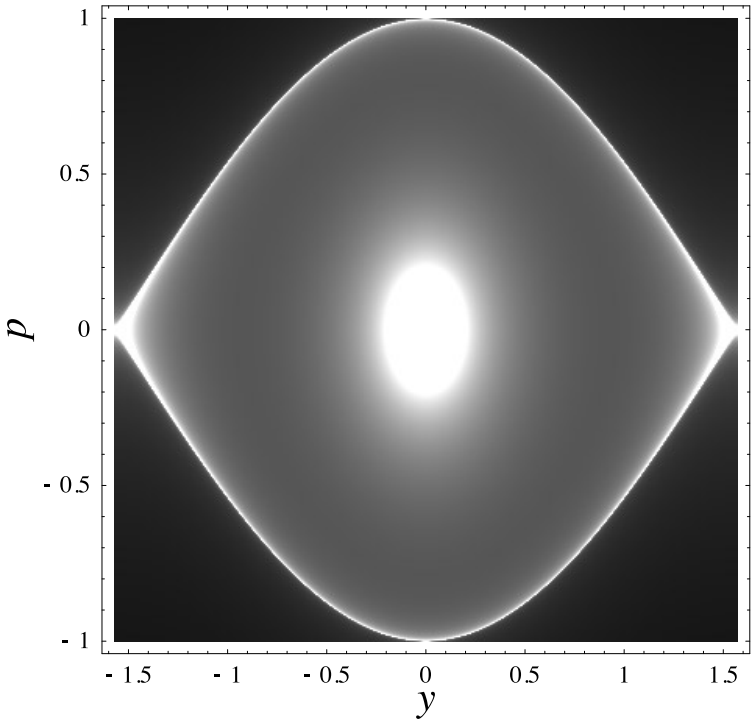

Figure 4. Density plot of 'classical Wigner function' (11).

(Θ denotes the unit step). Figure 4 shows this 'classical Wigner function'. There are singularities at the origin, where

$$W(y, p) \to \frac{1}{\pi^2\sqrt{p^2 + y^2}} \qquad (p^2 + y^2 \to 0) \tag{12}$$

and at the classical boundaries $|p| = \cos y$, where

$$W(y, p) \to \frac{1}{\pi \log\{8/[\cos y(\cos y - |p|)]\}\sqrt{2\cos y(\cos y - |p|)}} \qquad (|p| \to \cos y). \tag{13}$$

Third, W is averaged over y, to get the smoothed momentum density $I(p)$, normalized to unity:

$$\begin{aligned} I(p) &= \int_{-\pi/2}^{\pi/2} \mathrm{d}y\, W(y, p) \\ &= \frac{1}{2\pi}\int_{p^2}^{1} \frac{\mathrm{d}m}{K(m)\sqrt{m(1-m)(m-p^2)(1+p^2-m)}}. \end{aligned} \tag{14}$$

Figure 5 shows this function. There are logarithmic singularities at $p = 0$, where I diverges as

$$I(p) \to \frac{A}{\pi^2}\log\left(\frac{4}{p^2}\right) \qquad A \approx 1 \quad (p \to 0) \tag{15}$$

and at $p = 1$, where I vanishes as

$$I(p) \to \left[\log\left(\frac{16}{(1-|p|)}\right)\right]^{-1} \qquad (|p| \to 1). \tag{16}$$

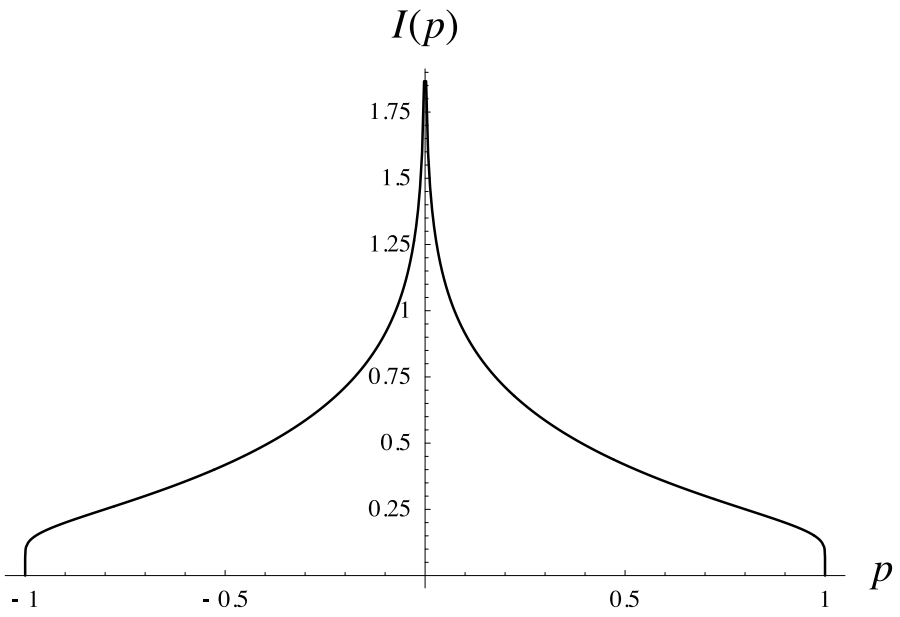

Figure 5. Ergodic momentum density (14).

4. Diffracted beam intensities

Waves traversing the volume grating with vacuum wavenumber k (and energy $E = \overline{h}^2k^2/2m$ for diffraction of particles with mass m) satisfy the Helmholtz equation

$$(\partial_\xi^2 + \partial_\eta^2 + k^2n^2(\eta))\psi(\xi, \eta) = 0. \tag{17}$$

For small n_1, wave propagation is paraxial. Thus, with the variables x, y (equation (4)), and the rescaled wavefunction Ψ, defined by

$$\psi(\xi, \eta) \equiv \exp(\mathrm{i}kn_0\xi)\Psi(x, y) \tag{18}$$

the term in $\partial_x^2\Psi$ can be dropped, and Ψ satisfies the paraxial wave equation

$$\mathrm{i}\sqrt{\rho}\partial_x\Psi(x, y) = (-\tfrac{1}{8}\rho\partial_y^2 - \cos(2y))\Psi(x, y) \tag{19}$$

involving the wave parameter

$$\rho \equiv \frac{q^2}{n_1n_0k^2}. \tag{20}$$

The short-wave (semiclassical) limit is $\rho \to 0$.

We note in passing that (19) has the form of a time-dependent Schrödinger equation: in terms of the effective Planck constant $\overline{h} = (\sqrt{\rho})/4$, momentum operator $p = -\mathrm{i}h\partial_y$, and Hamiltonian (6), (19) can be written

$$\mathrm{i}\overline{h}\partial_x\Psi = (H(x, y) - \tfrac{1}{4})\Psi. \tag{21}$$

The amplitudes $A_m(x)$ of diffracted beams emerging from the volume grating are the coefficients in the Fourier expansion (momentum representation) of Ψ:

$$\psi(x, y) = \sum_{m=-\infty}^{\infty} A_m(x)\exp(2\mathrm{i}my). \tag{22}$$

From (19), and the normal incidence condition, the amplitudes satisfy the differential-difference equation of Raman and Nath (1936):

$$2\mathrm{i}\sqrt{\rho}\partial_x A_m(x) = \rho m^2 A_m(x) - A_{m-1}(x) - A_{m+1}(x) \qquad A_m(0) = \delta_{m0}. \tag{23}$$

The diffracted beam intensities are (reinstating the dependence on ρ)

$$I_m(x;\rho) = |A_m(x)|^2. \tag{24}$$

The coupled equations (23) can be solved directly by numerical integration, or by diagonalizing the matrix on the right-hand side, whose eigenfunctions are Fourier coefficients of Mathieu functions (Berry 1966); analytical implementation of the second method leads to interesting asymptotics (O'Dell 1999).

For sufficiently small ρ, that is semiclassically, we expect the pattern of intensities I_m for fixed x to reflect the ray patterns in momentum space (figure 3). This approach has been used extensively, for oblique as well as normal incidence (Nomoto 1951a, b). Magnification of the calculated intensities near the caustic lines and cusp points in x, m space reveals the Airy and Pearcey diffraction patterns expected on the basis of catastrophe optics (Berry and Upstill 1980); we do not show these features here because they are unsurprising nowadays—and the fact that the diffraction catastrophes are sampled by a discrete variable (here m) is also not new (Berry 1975).

However, in the large-x limit we are pursuing here, detailed correspondence with the ray patterns fails, because of the proliferation of caustics. When these are close, the wave (Airy) pattern decorating each of them is obscured by overlap with those of its neighbours. This is an instance of a general phenomenon: breakdown of the wave-ray correspondence for long 'times', because the finite wavelength limits the ability to discern details of evolving classical structures as these get increasingly intricate (Berry 1983). (We do not address the related but incompletely resolved question of whether correspondence fails when interference between the contributing rays is incorporated—see Tomsovic and Heller (1991), and Schulman (1994) for a discussion of the presumably more difficult situation where the rays are chaotic.)

Even for large x, however, we expect the significant diffracted beams to be those, with $|m| \leqslant M(\rho)$, that lie within the range of ray directions. By considering the Bragg angle and ray deflections in the original (ξ, η) variables—or, alternatively, the spacing between eigenvalues of momentum $p = -\mathrm{i}[(\sqrt{\rho})/4]\partial_y$, we find

$$m_{\max}(\rho) = \frac{2}{\sqrt{\rho}}. \tag{25}$$

Figure 6 shows two sample patterns of diffracted beams, calculated for $\rho = 8 \times 10^{-5}$. Equation (25) gives $m_{\max}(\rho) = 100\sqrt{5} \approx 224$, in good agreement with the calculations. From the results of section 2, the corresponding ray patterns would involve about 60 caustics. We would not expect the diffraction patterns to resolve these, and clearly they do not. The only unambiguous correspondence is between the very large peak at the origin in figure 6(*a*) and the 30th cusp in the ray pattern. Otherwise, the diffraction patterns show a disorderly arrangement of peaks of different sizes.

However, we can compare averages of the diffraction intensities with the predictions (equation (14) and figure 5) of the ergodic theory. Figure 7 shows a momentum average of the intensities in figure 6(*b*). Evidently the ergodic theory captures the main features of the diffraction, but the averaging inevitably smooths the singularities of (14) at $p = 0$ and $|p| = 1$, and this discrepancy gets worse if the smoothing is increased to eliminate the diffraction oscillations.

For a more discriminating comparison, we need an x ('time') average. Figure 8 shows that the ergodic density, including its singularities, is reflected very accurately in the data. The

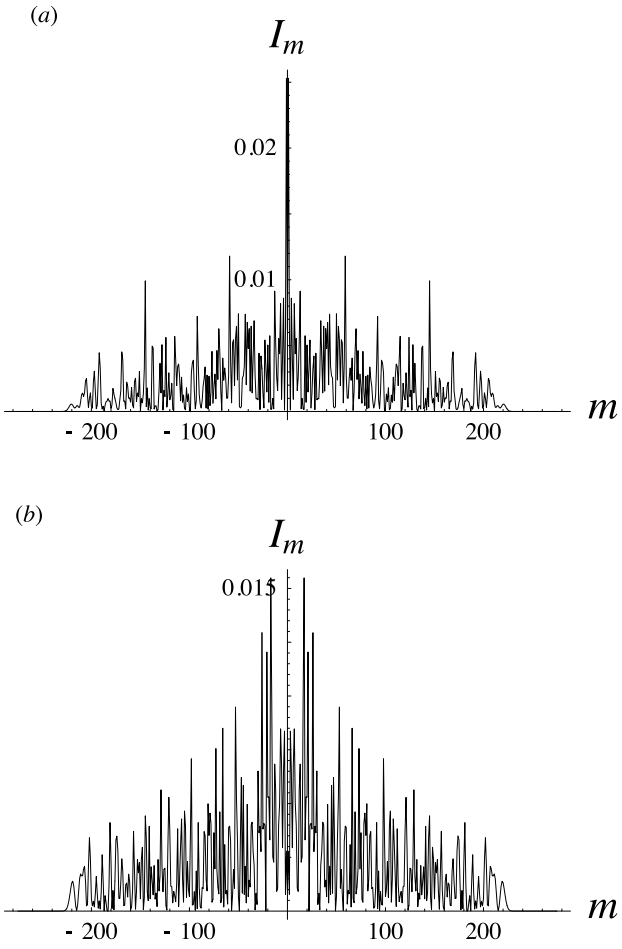

Figure 6. Diffracted beam intensities, calculated from (23) and (24) for $\rho = 8 \times 10^{-5}$ and (*a*) $x = 30\pi$, (*b*) $x = 30.5\pi$.

only diffraction oscillations not eliminated by averaging are near $p = 1$; these are associated with the Airy-function interference of the two rays connected with the extreme momentum caustic, which is always isolated and so uncontaminated by interference from other rays.

5. Fluctuations

Around the ergodic average, the intensities fluctuate wildly, both in m (figure 6) and x. As ρ decreases, the diffraction intensities should concentrate around the ray caustics, and the fluctuations should get stronger. They are an example of *singularity-dominated strong fluctuations* (Berry 1977, 1982, 1986). To characterize them, we define the moments

$$M_n(x;\rho) \equiv \sum_{m=-\infty}^{\infty} [I_m(x;\rho)]^n \tag{26}$$

and seek the leading-order ρ dependence of these moments as $\rho \to 0$.

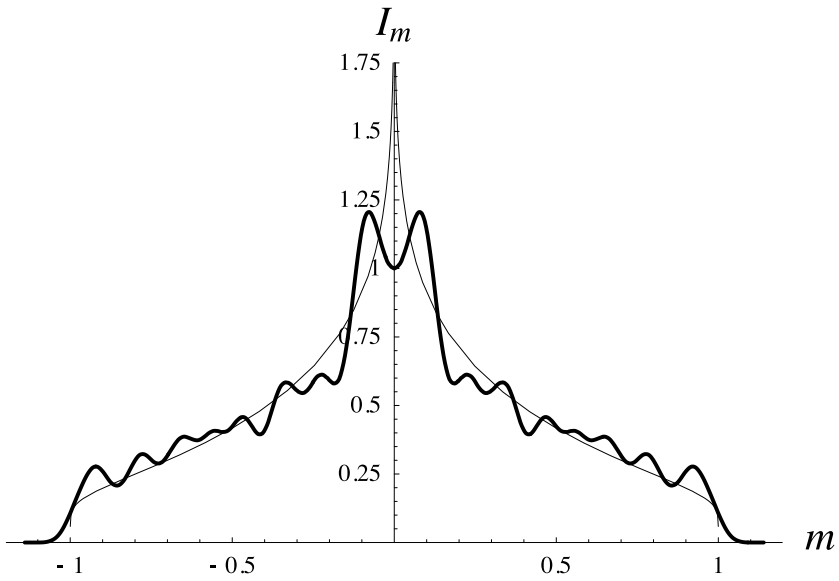

Figure 7. Thick line: Gaussian smoothing of the intensities in figure 6(*b*), with a rms width of 14 beams; thin line: ergodic momentum distribution (14), scaled to make $p_{\max} = 2/\sqrt{\rho}$.

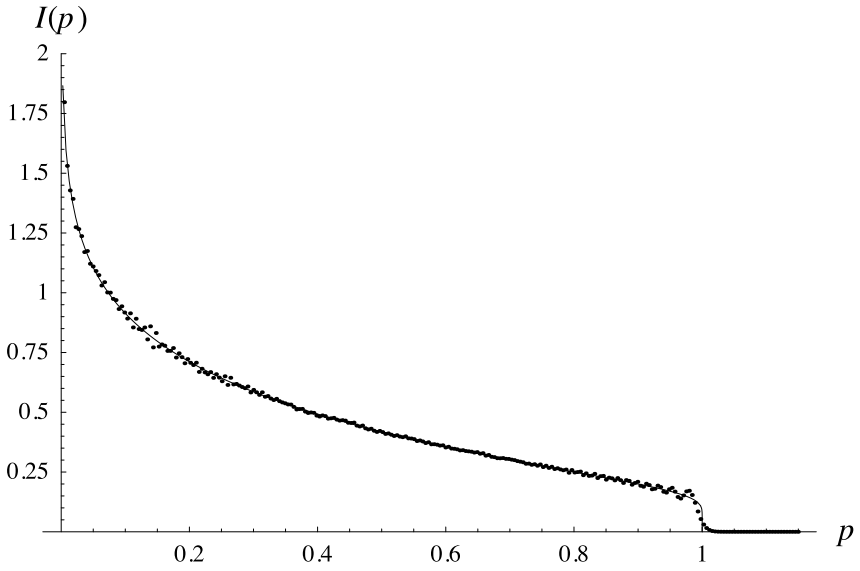

Figure 8. Dots: intensities I_m of diffracted beams averaged over the range $30\pi \leqslant x \leqslant 40\pi$, for $\rho = 8 \times 10^{-5}$, scaled and normalized in the range $-1 \leqslant p \leqslant 1$; full curve: ergodic momentum density (14).

In the calculation of this dependence, it is convenient when ρ is small to regard I_m as a discrete sampling of a diffraction function $I(p)$ of the continuous momentum variable p (we

suppress the x and ρ dependence). Sums and integrals are related by normalization

$$1 = \sum_{m=-\infty}^{\infty} I_m = \int_{-1}^{1} \mathrm{d}p\, I(p) \approx \frac{1}{m_{\max}(\rho)} \sum_{m=-\infty}^{\infty} I\left(\frac{m}{m_{\max}(\rho)}\right) \tag{27}$$

with $m_{\max}(\rho)$ given by (25). Thus

$$I_m \approx \frac{\sqrt{\rho}}{2} I(p) \tag{28}$$

and the moments are

$$M_n = \left(\frac{\rho}{4}\right)^{(n-1)/2} \int_{-1}^{1} \mathrm{d}p\, (I(p))^m. \tag{29}$$

For $m > 1$ and ρ small, the integral of $I(p)$ will be dominated by caustics, in ways well understood, and applied to the calculation of wavefunction moments by Berry *et al* (1983). If x is not close to a multiple of π, the caustics are the smooth fold catastrophe curves (figure 1(*b*)). Near each of these, $I(p)$ rises to values of order (wavelength)$^{-1/3}$ in a p interval of size (wavelength)$^{2/3}$ (Berry and Upstill 1980). From (20), the wavelength is proportional to ρ. Thus the integral in (29) can be estimated, giving the moments

$$M_n^{\mathrm{fold}} \propto \rho^{(n-1)/2} \rho^{-(n-2)/6}. \tag{30}$$

By contrast, the sum of nth powers of $2m_{\max} + 1$ independent random variables s_i, normalized so that their size is of order $1/m_{\max}$, is

$$\sum_{-m_{\max}}^{m_{\max}} (s_i)^n \propto m_{\max}^{-(n-1)} \propto \rho^{(n-1)/2}. \tag{31}$$

Comparing with (30), we see that the fluctuations associated with caustics are much stronger.

If x is a multiple of π, the integral over p is dominated by crossings of cusps (figure 1(*b*)), where the catastrophe scalings are different: $I(p)$ rises to values of order (wavelength)$^{-1/2}$ in a p interval of size (wavelength)$^{1/2}$. Thus (30) is replaced by

$$M_n^{\mathrm{cusp}} \propto \rho^{(n-1)/2} \rho^{-(n-1)/4} \tag{32}$$

from which it is clear that the fluctuations associated with cusps are greater than those at fold caustic curves.

Our numerical explorations of these predicted ρ scalings of the moments are at an early stage. When x is not large, we have seen the emergence of the power-laws (30) and (32) as ρ gets smaller. But when $x > \pi$ the overlap of diffraction fringes associated with different caustics slows down the asymptotics, requiring values of ρ so small (less than 10^{-12}) that special methods (O'Dell 1999) must be employed to solve the Raman–Nath equation.

References

Abramowitz M and Stegun I A 1972 *Handbook of Mathematical Functions* (Washington, DC: National Bureau of Standards)

Adams C S, Sigel M and Mlynek J 1994 Atom optics *Phys. Rep.* **240** 143–210

Berry M V 1966 *The Diffraction of Light by Ultrasound* (New York: Academic)

——1975 Cusped rainbows and incoherence effects in the rippling-mirror model for particle scattering from surfaces *J. Phys. A: Math. Gen.* **8** 566–84

——1977 Focusing and twinkling: critical exponents from catastrophes in non-Gaussian random short waves *J. Phys. A: Math. Gen.* **10** 2061–81

——1982 Universal power-law tails for singularity-dominated strong fluctuations *J. Phys. A: Math. Gen.* **15** 2735–49

——1983 *Les Houches Lecture Series* vol 36, ed G Iooss, R H G Helleman and R Stora (Amsterdam: North-Holland) pp 171–271

——1986 *Wave Propagation and Scattering* ed B J Uscinsci (Oxford: Clarendon) pp 11–35
Berry M V and Balazs N L 1979 Evolution of semiclassical quantum states in phase space *J. Phys. A: Math. Gen.* **12** 625–42
Berry M V, Hannay J H and Ozorio de Almeida A M 1983 Intensity moments of semiclassical wavefunctions *Physica* D **8** 229–42
Berry M V and Upstill C 1980 Catastrophe optics: morphologies of caustics and their diffraction patterns *Prog. Opt.* **18** 257–346
Ellison J A and Guinn T 1976 Statistical equilibrium, planar channelling, and the continuum model *Phys. Rev.* B **13** 1880–3
Lucas M and Biquard P 1932 Propriétés optiques des milieux solides et liquides soumis aux vibrations élastiques ultra sonores *J. Phys. Radium* **3** 464–77
Nomoto O 1951a Geometrical optical theory of the diffraction of light by ultrasonic waves. (1) Approximate treatment *Bull. Kobayasi Inst. Phys. Res.* **1** 42–71
——1951b Geometrical optical theory of the diffraction of light by ultrasonic waves. (2) Approximate treatment (2) *Bull. Kobayasi Inst. Phys. Res.* **1** 189–220
O'Dell D H J 1999 to be published
Raman C V and Nath N S N 1936 The diffraction of light by high frequency sound waves: part IV, generalised theory *Proc. Indian Acad. Sci.* A **3** 119–25
Schulman L S 1994 Accuracy of the semiclassical approximation for the time dependent propagator *J. Phys. A: Math. Gen.* **27** 1703–21
Tomsovic S and Heller E J 1991 Semiclassical dynamics of chaotic motion: unexpected long time accuracy *Phys. Rev. Lett.* **67** 664–7